



HAL
open science

Controls on the seafloor exposure of detachment fault surfaces

Jean-Arthur Olive, Ross Parnell-Turner, Javier Escartin, Deborah Smith,
Sven Petersen

► **To cite this version:**

Jean-Arthur Olive, Ross Parnell-Turner, Javier Escartin, Deborah Smith, Sven Petersen. Controls on the seafloor exposure of detachment fault surfaces. *Earth and Planetary Science Letters*, 2019, 506, pp.381-387. 10.1016/j.epsl.2018.11.001 . hal-02324084

HAL Id: hal-02324084

<https://hal.science/hal-02324084>

Submitted on 21 Oct 2019

HAL is a multi-disciplinary open access archive for the deposit and dissemination of scientific research documents, whether they are published or not. The documents may come from teaching and research institutions in France or abroad, or from public or private research centers.

L'archive ouverte pluridisciplinaire **HAL**, est destinée au dépôt et à la diffusion de documents scientifiques de niveau recherche, publiés ou non, émanant des établissements d'enseignement et de recherche français ou étrangers, des laboratoires publics ou privés.

Controls on the seafloor exposure of detachment fault surfaces

Jean-Arthur Olive^{1*}, Ross Parnell-Turner^{2,3}, Javier Escartín⁴, Deborah K. Smith⁵, and Sven Petersen⁶

¹*Laboratoire de Géologie, Ecole Normale Supérieure / CNRS UMR 8538, PSL Research University, 24 rue Lhomond, 75005, Paris, France.*

²*Woods Hole Oceanographic Institution, 266 Woods Hole Rd., Woods Hole MA, 02543, USA.*

³*Now at: Scripps Institution of Oceanography, Institute of Geophysics and Planetary Physics, University of California, San Diego, La Jolla, CA 92093, USA*

⁴*Institut de Physique du Globe de Paris – CNRS UMR 7154, 1 rue Jussieu, 75005, Paris, France.*

⁵*National Science Foundation, 2415 Eisenhower Ave., Alexandria, VA, 22314, USA.*

⁶*GEOMAR / Helmholtz Centre for Ocean Research, Wischhofstrasse 1-3, 24148, Kiel, Germany.*

*Corresponding author: olive@geologie.ens.fr

Keywords

Mid-ocean ridge; detachment faulting; oceanic core complex; critical taper; fault friction;

Highlights

- A small fraction of corrugated detachment fault surfaces is eventually exposed at the seafloor.
- Seafloor slopes indicate effective friction of ~0.15 on shallow part of detachments.
- Moderate-offset detachment faults may be largely blanketed by hanging wall material.
- Seafloor-shaping processes profoundly alter the morphology of oceanic core complexes.

29 **Abstract**

30 While oceanic detachment faults have been proposed to account for the accretion of ~40% of new
31 seafloor in the North Atlantic ocean, clear exposures of large-offset, often-corrugated fault
32 surfaces remain scarce and spatially limited. To help resolve this paradox, we examine the
33 conditions under which detachment fault growth may or may not lead to extensive exposure of
34 corrugated fault planes at the seafloor. Using high-resolution bathymetry from four detachment
35 faults at the northern Mid-Atlantic Ridge, we investigate the rafting of hanging wall-derived debris
36 over emerging fault scarps, which can lead to covering shallow-dipping corrugated fault surfaces.
37 We model this process using critical taper theory, and infer low effective friction coefficients
38 (~0.15) on the shallowest portion of detachment faults. A corollary to this result is that detachments
39 emerging from the seafloor at angles $<10^\circ$ are more likely to become blanketed under an apron of
40 hanging wall material. We generalize these findings as a simple model for the progressive exposure
41 and flexural rotation of detachment footwalls, which accounts for the continued action of seafloor-
42 shaping processes. Our model suggests that many moderate-offset, hidden detachment faults may
43 exist along slow mid-ocean ridges, and do not feature an exposed fault surface.

44

45 **1. Introduction**

46 Bathymetric highs composed of mafic and ultramafic units are a characteristic feature of slowly
47 accreted seafloor. These massifs are often capped by corrugated slip surfaces that represent the
48 rotated footwalls of detachment faults with offsets on par with or greater than the thickness of
49 young oceanic lithosphere (Cann et al., 1997; Tucholke et al., 1998; Parnell-Turner et al., 2018).
50 These faults are generally found on ridge sections characterized by greater-than-average seismicity
51 rates, lava geochemistry indicative of deeper fractionation, and hydrothermal activity (deMartin et
52 al., 2007; McCaig et al., 2007; Escartín et al., 2008b; Blackman et al., 2011; Wilson et al., 2013;
53 Olive and Escartín, 2016). Such observations led Escartín et al. (2008b) to postulate that
54 detachment faulting enables a distinct mode of asymmetric seafloor spreading, favored wherever
55 the magma supply of a mid-ocean ridge is subdued (Buck et al., 2005; Tucholke et al., 2008; Olive
56 et al., 2010).

57 Significant portions of seafloor in the North Atlantic ocean are presently forming through
58 asymmetric spreading (Escartín et al., 2008b; Cann et al., 2015). However, seafloor exposures
59 of corrugated fault surfaces, a telltale sign of detachment fault growth (Cann et al., 1997), are often

60 spatially confined (≤ 10 km along-axis; Fig. 1) and only make up a small fraction of the > 40 km-
61 long asymmetric sections of slow-spreading ridges. One explanation may be that detachment faults
62 underlie entire ridge segments but are only exposed in areas where hanging wall rider blocks
63 cannot develop (Smith et al., 2008; Reston and Ranero, 2011). Another is that detachment faults
64 have a limited along-axis extent and connect with shorter-offset faults through complex relay
65 structures (Smith et al., 2008; Tian and Choi, 2017). This debate warrants an improved
66 understanding of how various seafloor-shaping processes modulate the exposure of pristine slip
67 surfaces during detachment fault growth. These processes include gravitational mass wasting,
68 which can both erode and cover portions of the footwall (Cannat et al., 2013), as well as rafting of
69 hanging wall material onto the footwall. Here we investigate the mechanical and geometrical
70 factors that lead to covering an emerging detachment surface under a hanging wall apron, making
71 large-offset fault surfaces difficult to detect in shipboard bathymetric data. We then assess the
72 relative impact of hanging wall rafting and mass wasting on the shape of oceanic detachment faults.

73

74 **2. Seafloor morphology near oceanic detachment faults**

75 Fig. 1 shows high-resolution (< 2 m) bathymetry acquired using autonomous underwater vehicles
76 at four detachment faults along the Northern Mid-Atlantic Ridge: $13^{\circ}20'N$ (Escartín and Petersen,
77 2017; Escartín et al., 2017), $16^{\circ}36'N$ and South Core Complex (SCC; Smith et al., 2014), and the
78 Trans-Atlantic Geotraverse (TAG) detachment (Petersen et al., 2016). Geological interpretations
79 of bathymetric features and textures, combined with in-situ observations at $13^{\circ}20'N$, suggest a
80 common sequence of morphological domains at these detachments. The footwall cut-off scarp
81 (i.e., the breakaway high marking the initial location of fault emergence) is often texturally rough
82 (e.g., Fig. 1C), which is interpreted as the result of extensive gravitational mass wasting (Escartín
83 et al., 2017). Towards the ridge axis, this chaotic terrain gradually transitions into the corrugated
84 fault surface (Fig. 1A–D). This transition marks the place where angular blocks and talus stripped
85 from the breakaway ridge no longer blanket freshly exposed corrugated fault surfaces. This
86 difference is likely because the initially steep surface of growing detachments eventually rotates
87 to gravitationally stable angles ($< 30^{\circ}$, Lavier et al., 1999), which are no longer prone to mass
88 wasting (Cannat et al., 2013; Smith et al., 2014; Escartín et al., 2017).

89 The spatial extent of exposed corrugated surfaces varies greatly from one detachment to
90 another. At the $13^{\circ}20'N$ and SCC detachments, for example, the corrugated terrain exceeds 10 km^2

91 and abruptly connects with a rougher region termed "apron", axis-ward of the bathymetric moat
92 that marks the fault termination or hanging wall cut-off (break in slope in Fig. 2). At 13°20'N the
93 apron consists of basaltic and diabase blocks in an unlithified matrix, and incorporates some
94 footwall-derived peridotite and gabbro (Escartín et al., 2017). The apron surface has a texture that
95 is distinct from the adjacent volcanic terrain covering the ridge axis, and in many instances is thin
96 enough for the underlying corrugations to be visible beneath (Fig. 1A–D; Fig. 3A). At TAG, the
97 apron spans an area wider than the corrugated surface (Fig. 1A), and is directly adjacent to the
98 chaotic terrain south of 26°09'N. This geometry suggests that the apron has the potential to blanket
99 large extents of the detachment surface when certain geometrical and rheological conditions are
100 met.

101

102 3. Detachment aprons as extensional Coulomb wedges

103 To understand how hanging wall material may be dragged onto the emerging fault surface, we
104 model the apron as a cohesionless, critical Coulomb wedge of seafloor slope α with friction angle
105 ϕ_0 (30°, appropriate for mafic lithologies) overlying a detachment fault of dip β and friction angle
106 ϕ_D (Fig. 3A, Davis et al., 1983; Dahlen, 1984; Xiao et al., 1991; Yuan et al., 2015). We specifically
107 use the critical wedge model of Yuan et al. (2015), which accounts for the possibility of fluid
108 overpressure in the detachment. The fundamental assumption of wedge models is that the state of
109 stress in the apron results from a balance between topographic and frictional forces and is on the
110 verge of failure everywhere in critical wedges. The assumption of a cohesionless material is
111 consistent with observations of the 13°20'N detachment suggesting that the apron consists of a
112 mixture of unconsolidated rubble and finer-grained materials (Escartín et al., 2017).

113 We describe the state of stress within the wedge using two quantities ψ_D and ψ_0 , which
114 denote the angles between the most compressive principal stress (σ_I) and the detachment and apron
115 surface, respectively. These are useful to determine potential slip lines within the apron, which are
116 expected to lie at $(\pm 45^\circ - \phi_0/2)$ from σ_I (Fig. 3A). By definition, the critical taper angle for the apron
117 verifies:

$$118 \quad \alpha + \beta = \psi_D - \psi_0 . \quad (1)$$

119 If the entire apron is on the verge of Mohr-Coulomb failure, then only certain values of α , ψ_D and
120 ψ_0 are admissible for a given β . These values verify the following set of implicit equations:

121
$$\frac{\sin \alpha'}{\sin \phi_0} - \sin(2\psi_0 + \alpha') = 0 \quad , \quad (2)$$

122 and

123
$$\sin(2\psi_D + \phi_D) - \frac{1 - \lambda_D}{1 - \lambda_0} \frac{\sin \phi_D}{\sin \phi_0} - \frac{\lambda_D - \lambda_0}{1 - \lambda_0} \sin \phi_D \cos 2\psi_0 = 0 \quad . \quad (3)$$

124 In equation (2), α' is defined as an angle verifying

125
$$\tan \alpha' = \frac{1 - \rho_f / \rho}{1 - \lambda_0} \tan \alpha \quad , \quad (4)$$

126 where λ_0 and λ_D denote the fluid pressure ratio in the apron and detachment, respectively. The fluid
127 pressure ratio is defined following Yuan et al. (2015) as

128
$$\lambda = - \frac{p_f - \rho_f g D}{\sigma_z + \rho_f g D} \quad , \quad (5)$$

129 with

130
$$\sigma_z = -\rho g z \cos \alpha - \rho_f g D \quad . \quad (6)$$

131 In equations (5) and (6), p_f is fluid pressure at a point located at a seafloor-normal distance z
132 beneath the apron surface (notation "D2" in Yuan et al., 2015). D is the water depth, and ρ and ρ_f
133 refer to the density of the apron material (2400 kg m⁻³) and of the fluid percolating within the apron
134 (1000 kg m⁻³). We assume that seawater easily percolates into the heavily damaged apron (Escartin
135 et al., 2017), and exerts a hydrostatic fluid pressure throughout the wedge, i.e., fluid pressure
136 increases downward in the wedge following a hydrostatic gradient. It can be shown that equation
137 (5) reduces to $\lambda = \rho_f / \rho$ under hydrostatic conditions (see Appendix A. of Yuan et al. 2015). The
138 fluid pressure ratio is thus set equal to 0.42 within the apron for the remainder of our study.

139 Equations (1-3) are formulated in terms of a residual function $F(\alpha, \psi_D, \psi_0) = 0$, and solved
140 with a Newton method for a range of β -values. The associated Jacobian ∇F is estimated using
141 centered finite difference with a step of 10⁻⁶ rad. Convergence is considered achieved when the
142 norm of the residual falls below 10⁻¹¹. Our initial guess is $\alpha = \phi_0 / 2$, $\psi_0 = 20^\circ$, and ψ_D set to either
143 20° or 120°, which are empirically found to promote convergence towards the upper or lower
144 branch of the envelope, respectively. For a given pair of fault friction and fault fluid pressure
145 values –which can be expressed as an effective fault friction μ_{eff} (Fig. 3A)– the slope of the apron
146 and the dip of the detachment must satisfy a set of equilibrium relations, plotted as stability
147 envelopes in Fig. 3B. A MATLAB[®] script *GetWedgeEnvelope.m* is provided as part of the
148 Supplementary Materials to generate stability envelopes (combinations of α and β) as a function

149 of ϕ_0 , ϕ_D , λ_0 , and λ_D . This function calls the subroutines *wedge_residual.m* (Residual function) and
150 *wedge_jacobianFD.m* (Jacobian approximation), which are also provided.

151 Estimates for apron slope and detachment fault dip were obtained along 89 profiles oriented
152 parallel to the spreading direction, crossing the hanging-wall cutoff (or moat; see Fig. 2 and
153 3A). High-resolution bathymetry was extracted along profiles spaced 100 m apart at the four study
154 locations (Fig. 1). The position of the hanging-wall cutoff and spatial extent of the moat was
155 identified in map-view, based upon the locus of change in bathymetric slope, and then used to
156 define the hanging wall, footwall, and moat sections along each profile (Fig. 2). The mean apron
157 slope was estimated for each profile using the slope of a linear least-squares fit to the bathymetry
158 calculated over a 500 m distance downslope from the hanging wall-side edge of the moat, hence
159 the moat itself is not included in the fit. The mean detachment fault dip was estimated using the
160 slope of a linear fit to the bathymetry calculated 800 m upslope from the footwall-side edge of the
161 moat. Uniform fitting lengths were chosen for consistency and to minimize the effects of local
162 changes in slope, while not allowing profiles to extend onto the chaotic or neovolcanic terrains.
163 The average apron slope across our detachments is $6.2 \pm 3.3^\circ$ (1 standard deviation), and the average
164 detachment dip right beneath the hanging wall cutoff is $13.8 \pm 2.5^\circ$.

165

166 **4. Low effective friction on the shallow part of oceanic detachment faults**

167

168 We follow a grid search approach to identify the value of μ_{eff} that best explains the observed pair
169 of $(\alpha, \beta > -\alpha)$ along 89 corrugation-parallel bathymetric transects at the four detachments shown
170 in Figs. 1 and 2. For each pair (α, β) , we construct 100 envelopes spanning values of $0.42 \leq \lambda_D \leq$
171 0.82 and $0 \leq \phi_D \leq 30^\circ$. Each point on these envelopes corresponds to a specific stress orientation,
172 which determines the orientation of possible slip lines (secondary faults) within the apron (Fig.
173 3A). We restrict our analysis to the upper branch of the envelopes, which predicts net extension in
174 the wedge. We retain the envelopes whose upper branch lies at the shortest distance to each (α, β)
175 pair, within an error of 2° (Fig. 3B). This set of best-fitting envelopes correspond to a narrow subset
176 of (λ_D, ϕ_D) space, and consequently to a narrow range of μ_{eff} values. We repeat this operation for
177 an entire grid of (α, β) values, to which we are able to assign a best fitting μ_{eff} with a typical error
178 of ± 0.01 , plotted in Fig. 4 and as colored dots for each profile in Fig. 1. For convenience, we also

179 provide a polynomial approximation for μ_{eff} as a function of (α, β) , in degrees, which is accurate
180 within the above error margin:

$$\begin{aligned} \mu_{eff} = & 0.008252 + 0.004973\beta - 0.003603\alpha \\ & + 0.00012\beta^2 + 1.026 \times 10^{-5}\alpha\beta + 7.116 \times 10^{-5}\alpha^2 \\ & - 1.853 \times 10^{-6}\beta^3 + 3.793 \times 10^{-7}\beta^2\alpha - 3.959 \times 10^{-6}\beta\alpha^2 \\ & - 2.385 \times 10^{-6}\alpha^3 \end{aligned} \quad (7)$$

182 The inversion procedure described above yields a range of μ_{eff} between 0.06 and 0.16, with
183 a mode at 0.14 (Fig. 4). Since the geometry of the detachment surface is concave-down, measuring
184 fault dip at the termination may underestimate the true dip of the detachment beneath the apron
185 region (Fig. 3A). Estimates of the sub-seafloor fault geometry (available only for TAG and
186 13°20'N: deMartin et al., 2007; Parnell-Turner et al., 2017) suggest that detachments may steepen
187 by at most $\sim 10^\circ$ across the apron (see section 5). Underestimating the average detachment dip
188 beneath the apron by $\sim 5^\circ$ would lead to underestimating the effective friction by ~ 0.04 . Fig. 4
189 provides a straightforward way to assess the effect of an underestimated detachment dip (e.g., by
190 translating the points towards the right by $\sim 5^\circ$).

191 Profiles located away from the center of detachments tend to yield lower μ_{eff} (Fig. 1), which
192 may be due to the termination strike being highly oblique to the spreading direction at these
193 locations owing to the three-dimensional fault morphology. By contrast, profiles oriented normal
194 to the termination (i.e., most compatible with the two dimensional nature of the critical wedge
195 model and often located in the central part of the detachment) commonly yield μ_{eff} values ranging
196 between 0.10 and 0.16, which we consider to be more reliable. Some short-wavelength apparent
197 variability in μ_{eff} directly reflects second-order tectonic features that offset the fault termination
198 and alter slopes (e.g., at SCC, N and S of 16.425°N, Fig. 1B). Our 2-D analysis is therefore unlikely
199 to resolve frictional heterogeneities on a given detachment, if present.

200 Low values of effective friction are consistent with the common inference that the low
201 strength of detachment faults enables their longevity (Escartín et al., 1997). Our strength estimates
202 are however only representative of the uppermost ~ 1 km portion of detachments, which may be
203 different from the rest of the fault. A possible manifestation of this difference could be the lack of
204 shallow (≤ 3 km) microseismicity beneath TAG (deMartin et al., 2007) and 13°20'N (Parnell-
205 Turner et al., 2017), as recorded by local ocean bottom seismometers (OBS) arrays. While low
206 effective friction on compressional décollements is typically attributed to elevated fluid pressure

207 (e.g., Dahlen, 1984), such a scenario may be harder to envision in a tensional regime where cracks
208 and pores are likely well connected. If fluid pressure is hydrostatic within the detachment fault
209 zone, as was inferred by Hansen et al. 2013 for the Kane detachment down to depths of ~5 km,
210 then the true friction coefficient of the fault material must lie between ~0.17 and ~0.26 (Fig. 3A).
211 The precipitation of very weak minerals such as talc, with friction coefficients ranging between
212 ~0.05 and 0.23 (Moore and Lockner, 2008; Escartín et al., 2008a) in the fault zone has been
213 invoked as a key contributor to long-term strain localization (Escartín et al., 1997). By contrast,
214 invoking moderately weak clay minerals (with friction coefficients of ~0.4, e.g., Tesei et al., 2012)
215 to explain our estimates of effective friction would however require super-hydrostatic fluid
216 pressure ratios between 0.6 and 0.75. The 13°20'N detachment, however, does not feature extensive
217 weak phases (e.g., serpentinite, talc) and instead shows pervasive silicification (Bonnemains et al.,
218 2017). The low effective friction of detachments may instead have a non-lithological origin.
219 Episodes of seismic slip have been documented in the shallow, microseismically quiet portion of
220 the 13°20'N detachment (Craig and Parnell-Turner, 2017). It is possible that infrequent
221 earthquakes catastrophically reshape apron slopes to balance the low shear stresses that prevail
222 during seismic rupture. The temporally-averaged apron slopes we measure may thus be influenced
223 both by the long-term and the short-term fault strength, although this hypothesis is difficult to
224 evaluate with the available data.

225 The above reasoning relies on the assumption that the apron wedge is critically stable, i.e.,
226 sits on the stability envelope as shown in Fig. 3B. At the 13°20'N detachment, small escarpments
227 are visible in apron topography, potentially indicating secondary faulting (Fig. 3A). Internal wedge
228 deformation alone would be indicative of the unstable wedge regime (outside of the stability
229 envelope, Xiao et al., 1991). When coincident with slip on the detachment, secondary faulting
230 implies a critically-stable apron at 13°20'N. However, slip on other detachments may occur without
231 faulting in the apron. Such systems would plot inside the stability envelope. Since increasing
232 detachment friction shifts the stability boundary towards greater detachment dips (Hayman et al.
233 2003), one can identify the greatest value of detachment friction that allows a wedge of a given (α ,
234 β) to remain inside the stability envelope. This value corresponds to the critically-stable
235 configuration. In other words, the effective friction determined with our approach must be thought
236 of as an upper-bound on detachment strength.

237

238

239

240 **5. Implications for the seafloor exposure of detachment fault surfaces**

241 Regardless of the mechanistic interpretation for μ_{eff} , Coulomb wedge theory does predict
242 an effective value for detachment friction that explains apron architecture (including the pattern of
243 secondary faulting: Fig. 3A). A corollary to this model is that a detached piece of apron would not
244 remain affixed to the footwall if the fault emerges from the seafloor with a slope greater than \tan^{-1}
245 $(\mu_{eff}) \sim 6\text{--}9^\circ$, because the low basal shear stresses would not be able to counteract gravity. Pieces
246 of apron would thus slide back towards the hanging wall instead of blanketing the footwall.
247 Conversely, a detachment fault emerging from the seafloor with a slope $<9^\circ$ should be extensively
248 covered by hanging wall material.

249 The primary challenge in testing this idea is to infer detachment fault dip where it is not
250 exposed. Such estimates are possible at TAG and $13^\circ 20'N$, which constitute low and high end-
251 members for the extent of the corrugated fault surface, respectively, and have both been
252 instrumented with OBS arrays to illuminate the deeper portions of the fault zone through
253 microseismicity (deMartin et al., 2007; Parnell-Turner et al., 2017). The clouds of extensional
254 microseismicity observed at the roots of TAG and $13^\circ 20'N$ show dips as large as 70° at depths of
255 ~ 7 km below seafloor. This clearly indicates an overall concave-down geometry of the detachment
256 at depth. High-resolution seismic imaging studies will be needed to improve our knowledge of the
257 near-surface geometry of these detachments. In the meantime, seafloor slopes reveal that a large
258 portion of the apron domain at TAG is underlain by a detachment dipping with angles $\leq 10^\circ$ (Fig.
259 2A), which is not the case at $13^\circ 20'N$, where the fault emerges with slopes of $\sim 15^\circ$ (Fig. 2D). This
260 simple comparison supports the idea that a gently dipping detachment is prone to extensive
261 blanketing by apron material, and less likely to feature extensive, well exposed corrugated
262 surfaces.

263

264 **6. From covered to exposed detachment surfaces**

265 Seafloor shaping processes are strongly sensitive to slope. Gravitational mass wasting is favored
266 along slopes with an angle of repose steeper than $\sim 20\text{--}30^\circ$ (Cannat et al., 2013). By contrast,
267 blanketing of exposed fault surfaces by hanging wall material is favored for shallow slopes $<10^\circ$.
268 The emerging slope of a detachment fault is known to change as the footwall undergoes flexural

269 re-adjustment with continued slip (Buck, 1988; Lavier et al., 1999; Morris et al., 2009). Fig. 5
270 illustrates this process using an elastic model for footwall topography with increasing fault offset
271 (Buck, 1988; Schouten et al., 2010; Olive and Behn, 2014). In the early stages of detachment
272 growth, a breakaway ridge forms by slip along a high angle ($>30^\circ$) fault, which triggers the
273 extensive mass wasting that shapes the chaotic terrain (Fig. 5A). The morphology of young
274 detachments may thus be strongly determined by the competition between the rate of footwall
275 degradation by repeated rockslides, and the fault slip rate. Hence, efficient mass wasting could
276 very well bury short-offset corrugated surfaces under footwall-derived debris.

277 As fault offset increases, flexural rotation decreases the emerging detachment slope until
278 it becomes sub-horizontal (Fig. 5B). This stage favors extensive blanketing of the corrugated fault
279 surface by hanging wall material, as seen today at TAG, a detachment fault with only ~5 km of
280 offset (deMartin et al., 2007). Further extension on the detachment drives footwall doming (Fig.
281 5C), which increases the slope of the emerging footwall ($>10^\circ$) and shrinks the apron domain,
282 revealing an extensive corrugated surface (e.g., 13°20'N, with 9 km of offset). It should be noted
283 that the emergence angle will to some extent also reflect the amount of volcanic material extruded
284 onto the hanging wall (magmatic accretion in Fig. 5A).

285 Our model suggests that moderate-offset detachment faults may be widespread along slow-
286 spreading ridges but remain undetected by shipboard bathymetric surveys, as they are largely
287 blanketed by hanging wall material and do not (yet) expose large corrugated surfaces at the
288 seafloor. Extensive high-resolution bathymetric surveys and a better mechanistic description of
289 seafloor-shaping processes thus constitute crucial next steps to improve our understanding of slow-
290 spreading ridge tectonics.

291

292 **Acknowledgements**

293 The authors wish to thank the ODEMAR (doi:[10.17600/13030070](https://doi.org/10.17600/13030070)) and M127 Science Parties as
294 well as the teams operating the AUVs (WHOI's *Sentry* and GEOMAR's *Abyss*). JAO was funded
295 under NSF project EAR16500166. Cruise funding was provided through CNRS and IFREMER
296 (JE), and GEOMAR and the EU-FP7-Project “Blue Mining: Breakthrough Solutions for the
297 Sustainable Exploration and Extraction of Deep Sea Mineral Resources” under grant No. 604500
298 (SP). Xiaoping Yuan provided valuable guidance on the Coulomb wedge modeling. Finally, we

299 thank Nadaya Cubas, Nicholas Hayman, and an anonymous reviewer for their thoughtful
300 suggestions, which greatly improved our manuscript.

301

302 **References**

303 Blackman, D.K., et al., 2011, Drilling constraints on lithospheric accretion and evolution at
304 Atlantis Massif, Mid-Atlantic Ridge 30°N: *J. Geophys. Res.*, v. 116, no. B07103,
305 doi:10.1029/2010JB007931.

306 Bonnemains, D., Escartín, J., Mével, C., Andreani, M., and Verlaguet, A., 2017, Pervasive
307 silicification and hanging wall overplating along the 13°20'N oceanic detachment fault (Mid-
308 Atlantic Ridge): *Geochem. Geophys. Geosyst.*, v. 18, no. 6, p. 2028–2053,
309 doi:10.1002/2017GC006846.

310 Buck, W.R., 1988, Flexural Rotation of Normal Faults: *Tectonics*, v. 7, no. 5, p. 959–973, doi:
311 10.1029/TC007i005p00959.

312 Buck, W.R., Lavier, L., and Poliakov, A.N.B., 2005, Modes of faulting at mid-ocean ridges:
313 *Nature*, v. 434, p. 719–723, doi: 10.1038/nature03358.

314 Cann, J.R., Blackman, D.K., Smith, D.K., McAllister, E., Janssen, B., Mello, S., Avgerinos, E.,
315 Pascoe, A.R., and Escartin, J., 1997, Corrugated slip surfaces formed at North Atlantic ridge-
316 transform intersections: *Nature*, v. 385, p. 329–332.

317 Cann, J.R., Smith, D.K., Escartín, J., and Schouten, H., 2015, Tectonic evolution of 200 km of
318 Mid-Atlantic Ridge over 10 million years — Interplay of volcanism and faulting: *Geochem.*
319 *Geophys. Geosyst.*, v. 16, p. 2303–2321, doi:10.1002/2015GC005797.

320 Cannat, M., Mangeney, A., Ondréas, H., Fouquet, Y., and Normand, A., 2013, High-resolution
321 bathymetry reveals contrasting landslide activity shaping the walls of the Mid-Atlantic Ridge
322 axial valley: *Geochem., Geophys., Geosyst.*, v. 14, no. 4, p. 996–1011,
323 <http://doi.org/10.1002/ggge.20056>.

324

325 Craig, T.J., Parnell-Turner, R., 2017. Depth-varying seismogenesis on an oceanic detachment fault
326 at 13°20'N on the Mid-Atlantic Ridge. *Earth Planet. Sci. Lett.*, v. 479, p. 60–70,
327 doi:10.1016/j.epsl.2017.09.020.

328

329 Collins, J.A., Smith, D.K., and McGuire, J.J., 2012, Seismicity of the Atlantis Massif detachment
330 fault, 30°N at the Mid-Atlantic Ridge: *Geochem. Geophys. Geosyst.*, v. 13, no. 1, p.
331 doi:10.1029/2012GC004210, doi: 10.1029/2012GC004210.

332 Dahlen, F.A., 1984, Noncohesive critical Coulomb wedges: An exact solution: *J. Geophys. Res.*,
333 v. 89, no. B12, p. 10,215–10,033.

334 Davis, D., Suppe, J., and Dahlen, F.A., 1983, Mechanics of fold-and-thrust belts and accretionary
335 wedges: *J. Geophys. Res.*, v. 88, no. B2, p. 1153–1172.

336 deMartin, B. J., Sohn, R.A., Canales, J.P., and Humphris, S.E., 2007, Kinematics and geometry of
337 active detachment faulting beneath the Trans-Atlantic Geotraverse (TAG) hydrothermal field
338 on the Mid-Atlantic Ridge: *Geology*, v. 35, p. 711–714, doi: 10.1130/G23718A.1.

339 Escartín, J., Hirth, G., and Evans, B., 1997, Effects of serpentinization on the lithospheric strength
340 and the style of normal faulting at slow-spreading ridges: *Earth Planet. Sci. Lett.*, v. 151, no.
341 3–4, p. 181–189, doi:10.1016/S0012-821X(97)81847-X.

342

343 Escartín, J., Andreani, M., Hirth, G., and Evans, B., 2008a, Relationships between the
344 microstructural evolution and the rheology of talc at elevated pressures and temperatures: *Earth*
345 *Planet. Sci. Lett.*, v. 268, p. 463–475.

346

347 Escartín, J., Smith, D.K., Cann, J.R., Schouten, H., Langmuir, C.H., and Escrig, S., 2008b, Central
348 role of detachment faults in accretion of slow-spreading oceanic lithosphere: *Nature*, v. 455,
349 no. 7214, p. 790–794, doi: 10.1038/nature07333.

350 Escartín, J., and Petersen, S., 2017, ODEMAR AUV Abyss (GEOMAR) + shipboard Pourquoi
351 Pas? Multibeam bathymetry – 13°20'N and 13°30'N Oceanic Core Complexes, Mid-Atlantic
352 Ridge: SEANOE, <http://doi.org/10.17882/48335>.

353 Escartín, J., Petersen, S., Bonnemains, D., Cannat, M., Andreani, M., Bezos, A., Chavagnac, V.,
354 Choi, Y., Godard, M., Haaga, K., Hamelin, C., Ildefonse, B., Jamieson, J., John, B., et al.,
355 2017, Tectonic structure, evolution, and the nature of oceanic core complexes and their
356 detachment fault zones (13°20' N and 13°30'N, Mid Atlantic Ridge): *Geochem. Geophys.*
357 *Geosyst.*, 18, doi:10.1002/2016GC006775.

358 Hansen, L.N., Cheadle, M.J., John, B.E., Swapp, S.M., Dick, H.J.B., Tucholke, B.E., and Tivey,
359 M.A., 2013, Mylonitic deformation at the Kane oceanic core complex: Implications for the
360 rheological behavior of oceanic detachment faults: *Geochem. Geophys. Geosyst.*, 14,
361 doi:10.1002/ggge.20184.

362 Hayman, N.W., Knott, J.R., Cowan, D.S., Nemser, E., and Sarna-Wojnicki, A.M., 2003,
363 Quaternary low-angle slip on detachment faults in Death Valley, California: *Geology*, v. 31,
364 no. 4, p. 343–346.

365 Lavier, L., Buck, W.R., and Poliakov, A., 1999, Self-consistent rolling-hinge model for the
366 evolution of large-onset low-angle normal faults: *Geology*, v. 27, no. 12, p. 1127–1130, doi:
367 10.1130/0091-7613(1999)027<1127:SCRHMF>2.3.CO;2.

368 McCaig, A.M., Cliff, R.A., Escartín, J., Fallick, A.E., and MacLeod, C.J., 2007, Oceanic
369 detachment faults focus very large volumes of black smoker fluids: *Geology*, v. 35, no. 10., p.
370 935–938.

371 Moore, D.E., and Lockner, D.A., 2008, Talc friction in the temperature range 25°–400°C:
372 Relevance for fault-zone weakening: *Tectonophysics*, v. 449, p. 120-132,
373 doi:10.1016/j.tecto.2007.11.039.

374 Morris, A., Gee, J.S., Pressling, N., John, B.E., MacLeod, C.J., Grimes, C.B., and Searle, R.C.,
375 2009, Footwall rotation in an oceanic core complex quantified using reoriented Integrated
376 Ocean Drilling Program core samples: *Earth Planet. Sci. Lett.*, v. 287, no. 1–2, p. 217–228,
377 doi: 10.1016/j.epsl.2009.08.007.

378 Olive, J.-A., Behn, M.D., and Tucholke, B.E., 2010, The structure of oceanic core complexes
379 controlled by the depth-distribution of magma emplacement: *Nat. Geosci.*, v. 3., p. 491–495,

380 doi:10.1038/ngeo888.

381 Olive, J.-A., and Behn, M.D., 2014, Rapid rotation of normal faults due to flexural stresses: An
382 explanation for the global distribution of normal fault dips: *J. Geophys. Res.*, *119*,
383 doi:10.1002/2013JB010512.

384

385 Olive, J.-A., and Escartín, J., 2016, Dependence of seismic coupling on normal fault style along
386 the Northern Mid-Atlantic Ridge: *Geochem. Geophys. Geosyst.*, *17*, 4128–4152, doi:10.1002/
387 2016GC006460

388

389 Parnell-Turner, R., Escartín, J., Olive, J.A., Smith, D.K., Petersen, S., 2018. Genesis of corrugated
390 fault surfaces by strain localization recorded at oceanic detachments. *Earth Planet. Sci. Lett.*
391 *498*, 116–128. doi:10.1016/j.epsl.2018.06.034

392

393 Parnell-Turner, R., Sohn, R.A., Peirce, C., Reston, T.J., MacLeod, C.J., Searle, R.C., and Simão,
394 N.M., 2017, Oceanic detachment faults generate compression in extension: *Geology*,
395 doi:10.1130/G39232.1.

396

397 Petersen, S., and Shipboard Scientific Party, 2016, Cruise report M127 –Metal fluxes and Resource
398 Potential at the Slow-spreading TAG Mid-ocean Ridge Segment (26°N, MAR)– Blue
399 Mining@Sea: GEOMAR report 32, doi: 10.3289/GEOMAR_REP_NS_32_2016.

400

401 Reston, T.J., and Ranero C.R., 2011, The 3-D geometry of detachment faulting at mid-ocean
402 ridges: *Geochem. Geophys., Geosyst.*, v. 12, no. 7, doi:10.1029/2011GC003666.

403

404 Schouten, H., Smith, D.K., Cann, J.R., and Escartin, J., 2010, Tectonic versus magmatic extension
405 in the presence of core complexes at slow-spreading ridges from a visualization of faulted
406 seafloor topography: *Geology*, v. 38, no. 7, p. 615–618, doi: 10.1130/G30803.1.

407 Smith, D.K., Escartin, J., Schouten, H., and Cann, J.R., 2008, Fault rotation and core complex
408 formation: Significant processes in seafloor formation at slow-spreading mid-ocean ridges

409 (Mid-Atlantic Ridge, 13°–15°N): *Geochem. Geophys. Geosyst.*, v. 9, no. 3, p.
410 doi:10.1029/2007GC001699, doi: 10.1029/2007GC001699.

411 Smith, D.K., Schouten, H., Dick, H.J.B., Cann, J.R., Salters, V., Marschall, H.R., Ji, F., Yoerger,
412 D., Sanfilippo, A., Parnell-Turner, R., Palmiotto, C., Zheleznov, A., Bai, H., Junkin, W., et al.,
413 2014, Development and evolution of detachment faulting along 50 km of the Mid-Atlantic
414 Ridge near 16.5°N: *Geochem. Geophys. Geosyst.*, v. 15, p. 4692–4711,
415 doi:10.1002/2014GC005563.

416 Spencer, J.E., Reynolds, S.J., Scott, R.J., and Richard, S.M., 2016, Shortening in the upper plate
417 of the Buckskin-Rawhide extensional detachment fault, southwestern U.S., and implications
418 for stress conditions during extension: *Tectonics*, v. 35, no. 12, p. 3119–3136,
419 doi:10.1002/2016TC004345.

420 Tesei, T., Collettini, C., Carpenter, B.M., Viti, C., and Marone, C., 2012, Frictional strength and
421 healing behavior of phyllosilicate-rich faults: *J. Geophys. Res.*, v. 117,
422 doi:10.1029/2012JB009204.

423 Tian, X., and Choi, E., 2017, Effects of axially variable diking rates on faulting at slow spreading
424 mid-ocean ridges: *Earth Planet. Sci. Lett.*, v. 458, p. 14–21.

425 Tucholke, B.E., Lin, J., and Kleinrock, M.C., 1998, Megamullions and mullion structure defining
426 oceanic metamorphic core complexes on the Mid-Atlantic Ridge: *J. Geophys. Res.*, v. 103, no.
427 B5, p. 9857–9866.

428 Xiao, H.-B., Dahlen, F.A., and Suppe, J., 1991, Mechanics of extensional wedges: *J. Geophys.*
429 *Res.*, v. 96, no. B6, p. 301–318.

430 Wilson, S.C., Murton, B.J., and Taylor, R.N., 2013, Mantle composition controls the development
431 of an Oceanic Core Complex: *Geochem. Geophys. Geosyst.*, v. 14., no. 4, doi:
432 10.1002/ggge.20046

433 Yuan, X.P., Leroy, Y.M., and Maillot, B., 2015, Tectonic and gravity extensional collapses in
434 overpressured cohesive and frictional wedges: *J. Geophys. Res.*, v. 120,

435 doi:10.1002/2014JB011612.

436

437 **Figure captions**

438

439 **Figure 1.** A–D: Seafloor terrain and slopes at four Mid-Atlantic Ridge detachment faults (locations
440 shown in inset E), from AUV bathymetric data gridded at 2 m resolution and plotted at equal scale.
441 Colored dots mark detachment termination, color-coded by effective friction (see section 4). Red
442 arrows indicate spreading direction, pointing away from the ridge axis. Dashed lines show
443 northernmost and southernmost spreading-parallel profiles bracketing topographic profiles used
444 here, which are evenly spaced at 100 m. RR = rubble ridges, i.e., small fragments of broken-down
445 apron carried by the fault surface.

446

447 **Figure 2.** High-resolution bathymetric profiles oriented parallel to the transport direction (inferred
448 from corrugations), spaced 100 m apart between dashed lines in Fig. 1. Thin red/blue/black
449 sections are hanging wall / footwall / moat sections of each profile, respectively; thick gray lines
450 are linear fits used to obtain estimates for apron slope and detachment fault dip. A: TAG; B:
451 16°36'N OCC; C: South Core Complex; D: 13°20'N OCC.

452

453 **Figure 3.** A: Schematic cross section of the termination of the 13°20'N detachment fault, based on
454 topographic profile XX' from Fig. 1D. Inset shows a zoom on the hanging wall apron, with inferred
455 slip line orientations. Setup of corresponding critical taper model shown below. B: Stability
456 envelopes calculated using extensional taper model. These envelopes all account for slope of
457 13°20'N apron measured along crest profile, and all correspond to an effective friction coefficient
458 of $\mu_{eff} = 0.15 \pm 0.01$ on detachment fault.

459

460 **Figure 4.** Contours of best-fitting effective friction on a detachment fault of dip β underlying an
461 apron of slope α , assuming a critical taper model with hydrostatic fluid pressure and an internal
462 friction angle of 30°. Symbols indicate measured slopes along the profiles bracketed in Fig. 1. hc:
463 hanging wall cutoff (termination).

464

465 **Figure 5.** Progressive rollover and exhumation of a detachment fault. Blue curve is rolling hinge
466 model of Buck (1988) for an elastic plate of flexural wavelength L (~1 km at the MAR, Schouten
467 et al., 2010). A: At moderate offsets (e.g., fault heave = $2L$), footwall slopes are steep, which leads

468 to mass wasting of the breakaway (fc: footwall cutoff) region, eventually forming the chaotic
469 terrain. B: At intermediate offsets (e.g., fault heave = $3L$) flexural rotation of the footwall leads to
470 very shallow seafloor slopes, promoting a widespread apron zone burying most of the detachment
471 surface. C: Finally, at large offsets (e.g., fault heave = $4L$) late-stage doming occurs close to the
472 fault termination (hc: hanging wall cutoff) where seafloor slopes increase, reducing the extent of
473 the apron and exposing the corrugated detachment surface (wiggly lines).

Figure 1

[Click here to download Figure: Figure_1_OCC_maps_SMALL.pdf](#)

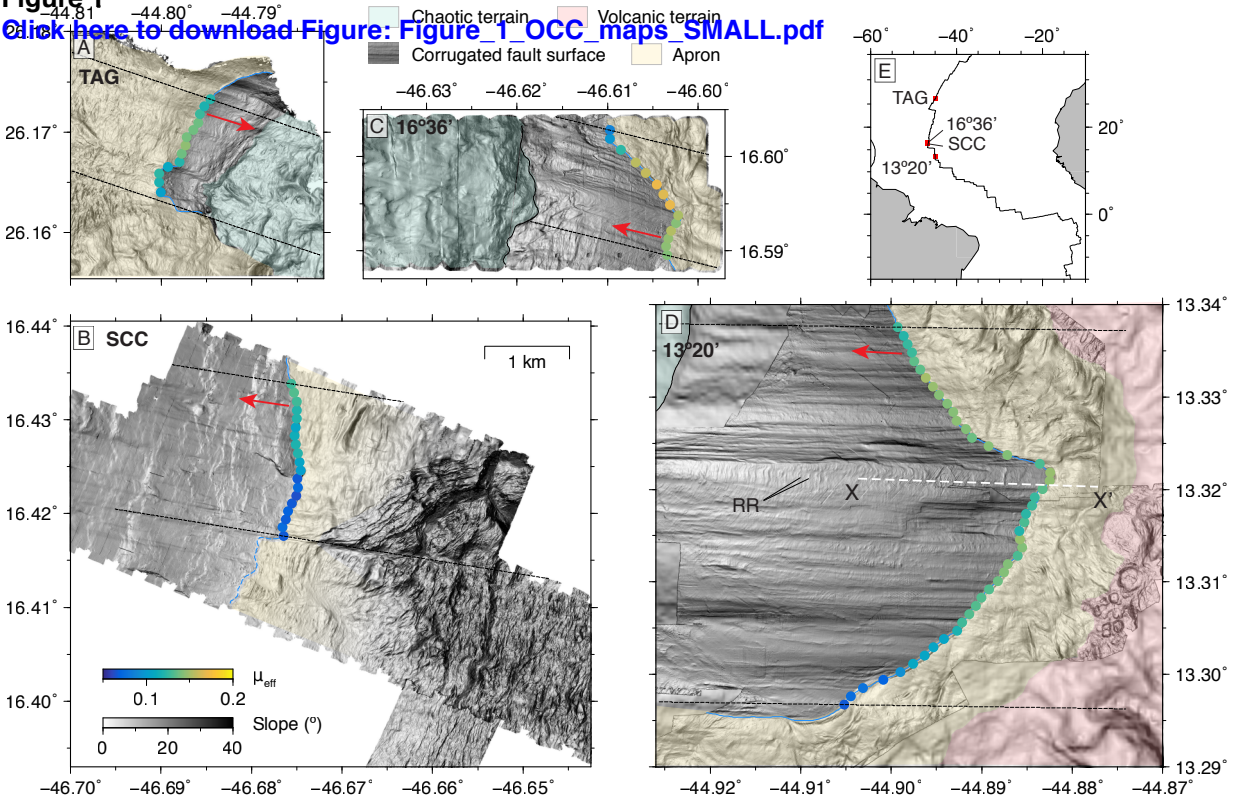


Figure 2

[Click here to download Figure: Figure_2_all slopes.pdf](#)

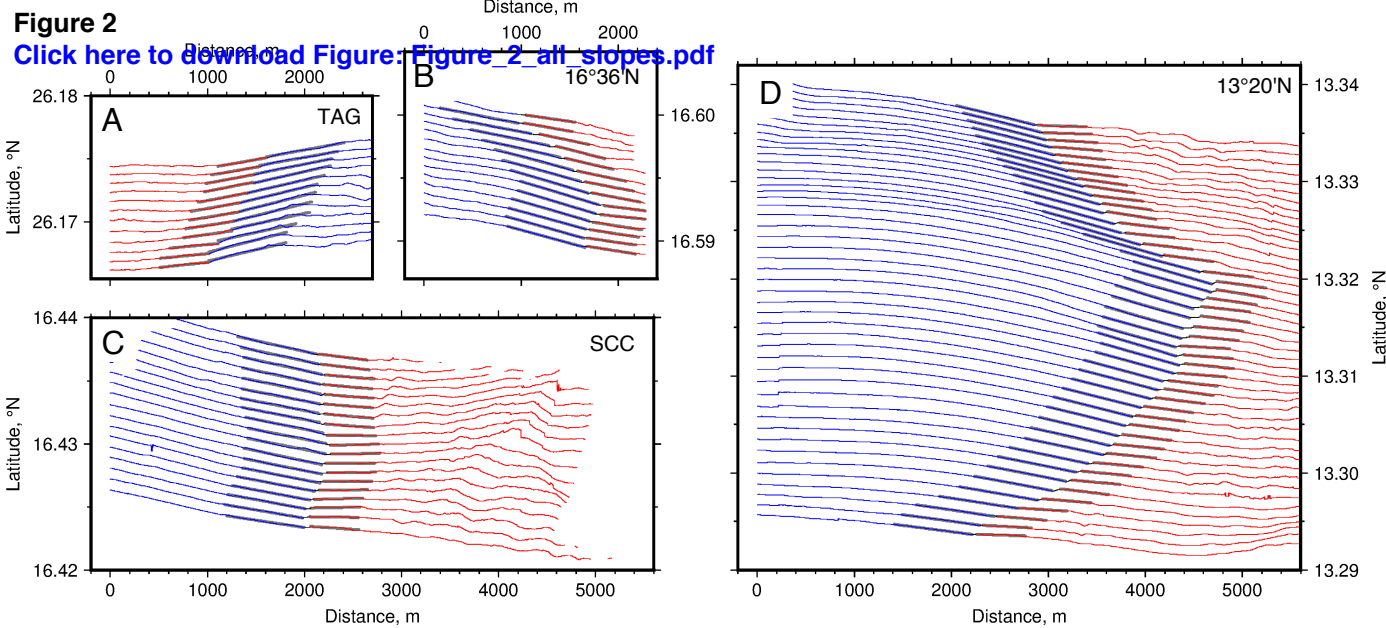
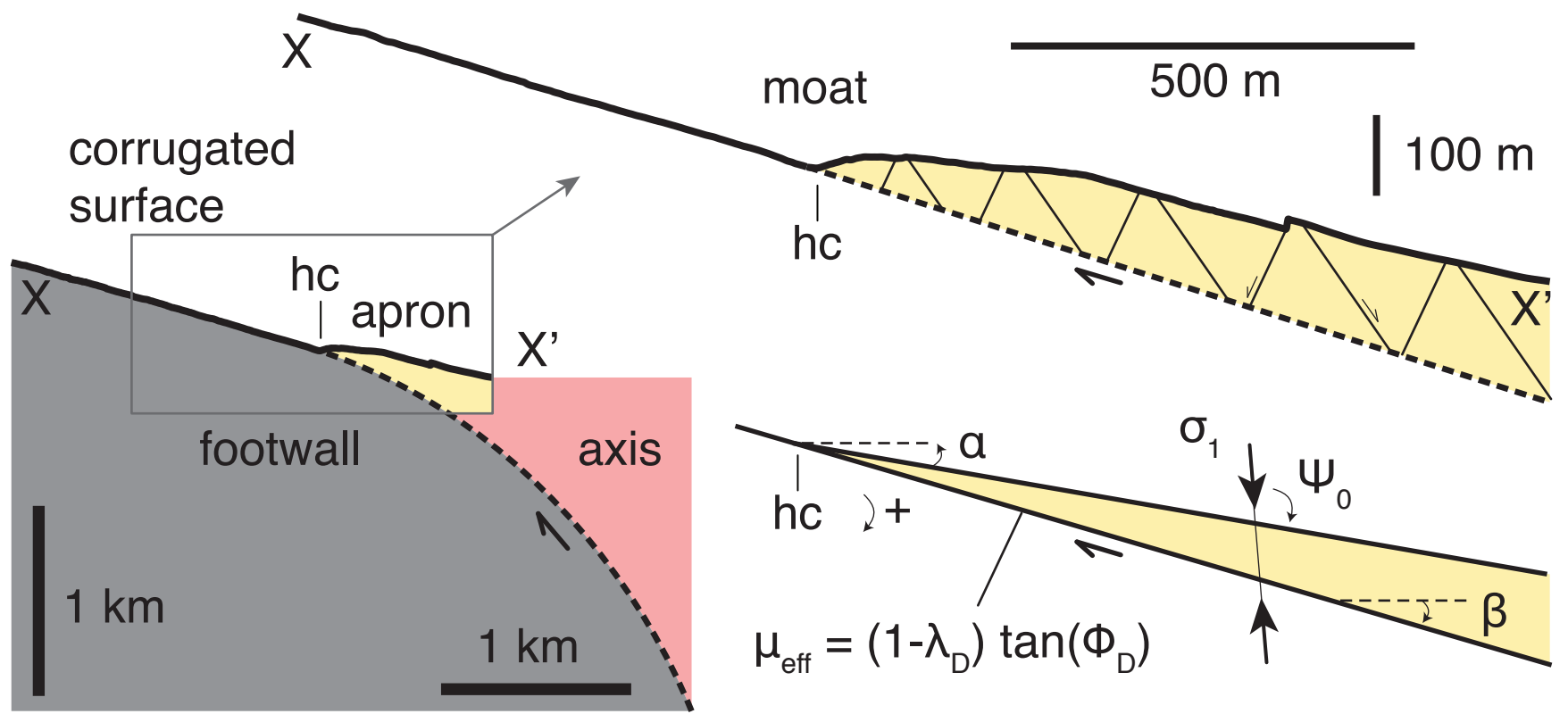


Figure 3
[Click here to download Figure: Figure_3_apron_model.pdf](#)



B

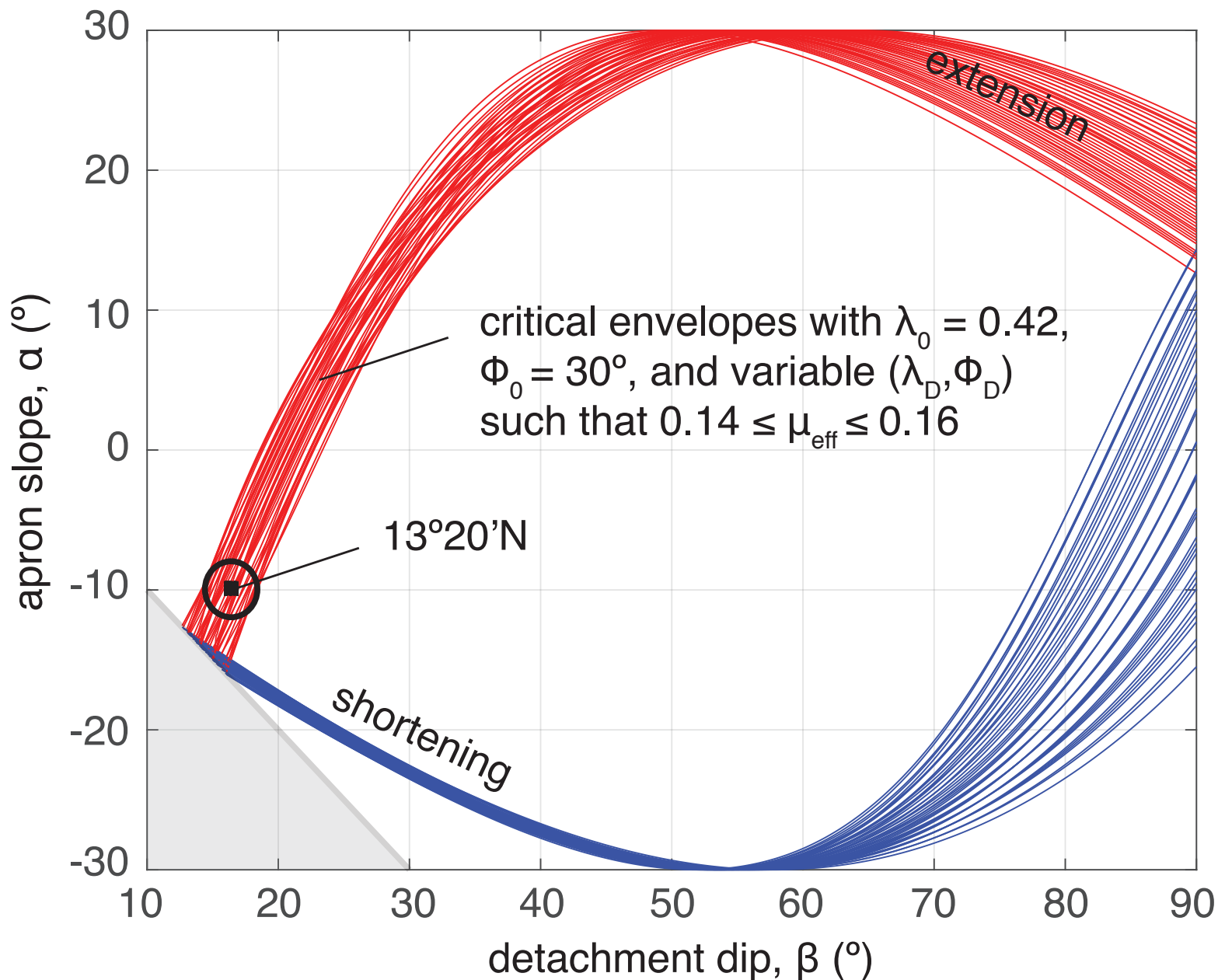


Figure 4

[Click here to download Figure: Figure_4_slopes2friction.pdf](#)

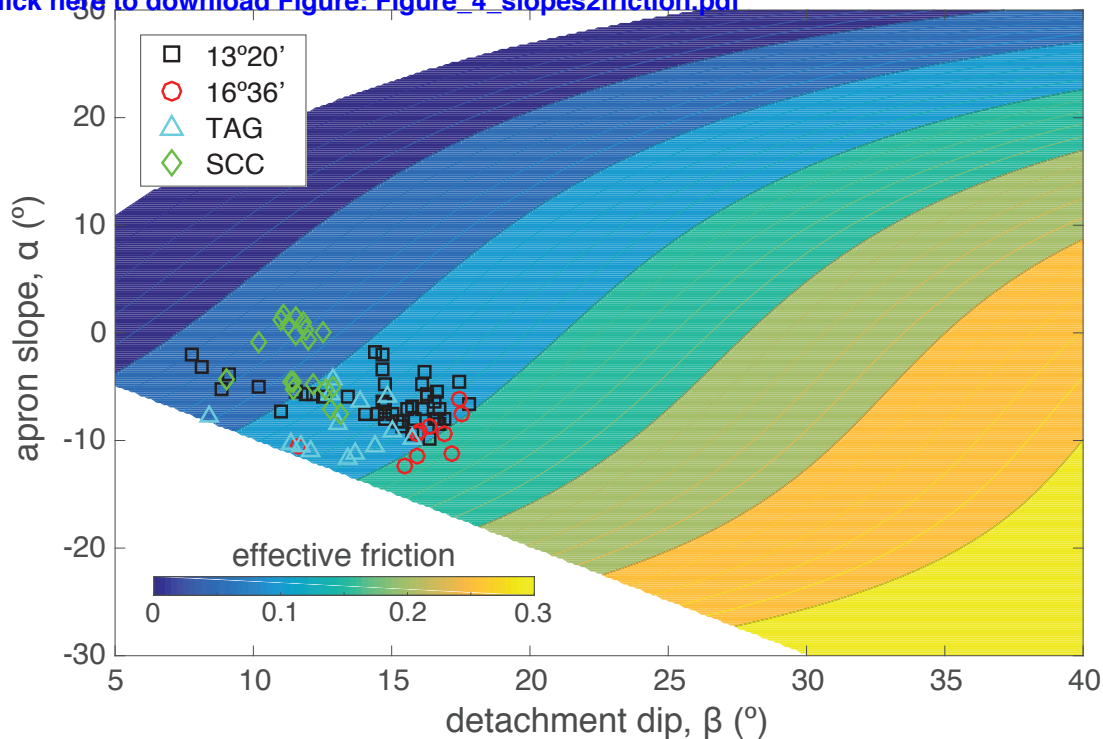


Figure 5
[Click here to download Figure: Figure_5_synthetic_cartoon.pdf](#)

